PHYSIOLOGICAL GENOMICS

VOLUME 24
APRIL 2006

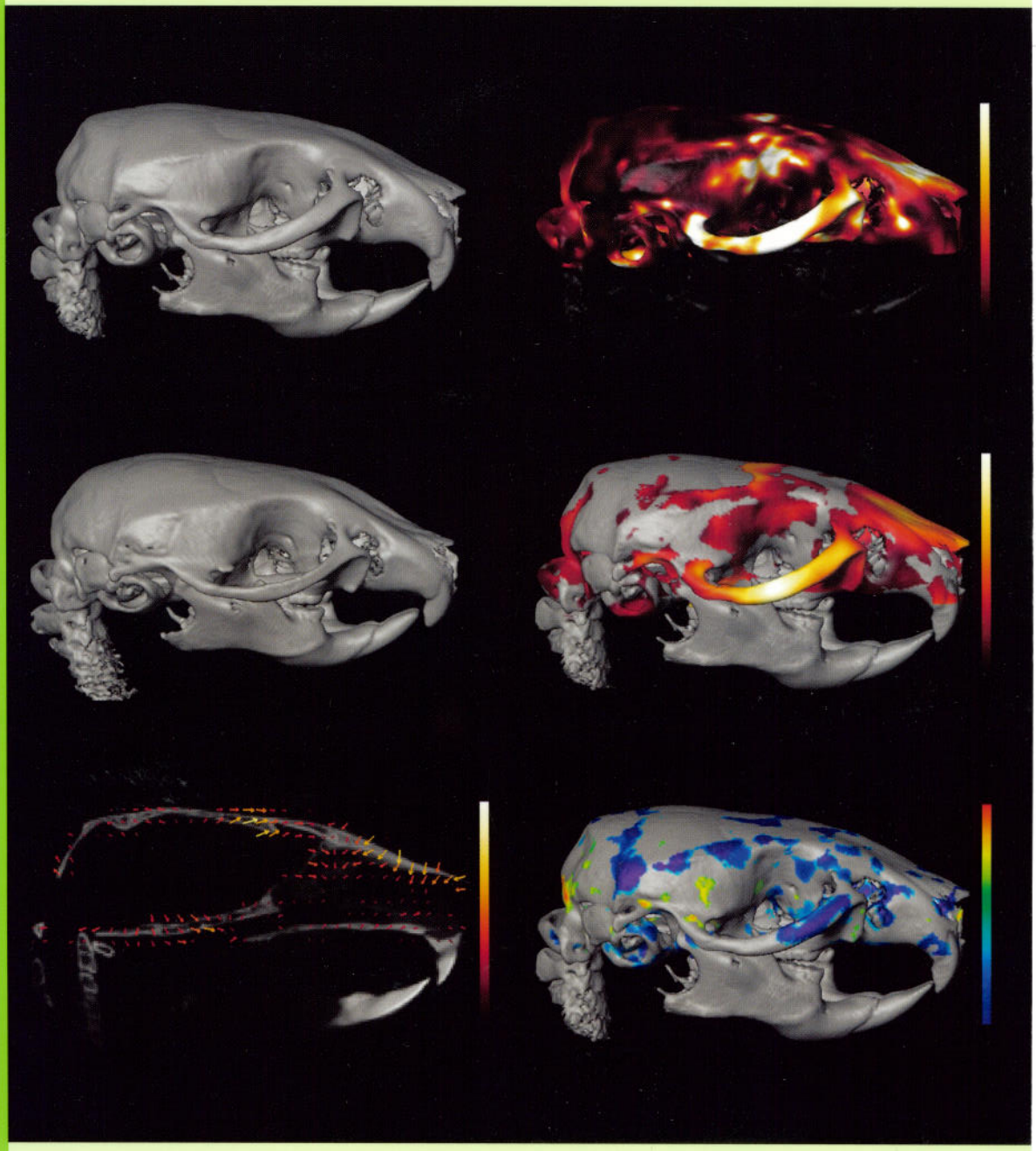

PUBLISHED BY THE AMERICAN PHYSIOLOGICAL SOCIETY
physiolgenomics.org

Physiol Genomics 24: 154–162, 2006;
doi:10.1152/physiolgenomics.00217.2005.

Anatomical phenotyping in the brain and skull of a mutant mouse by magnetic resonance imaging and computed tomography

Brian J. Nieman,[1,2] Ann M. Flenniken,[3] S. Lee Adamson,[3,4] R. Mark Henkelman,[1,2] and John G. Sled[1,2]

[1]*Mouse Imaging Centre, Hospital for Sick Children, Toronto;* [2]*Department of Medical Biophysics, University of Toronto, Toronto;* [3]*Centre For Modeling Human Disease, Samuel Lunenfeld Research Institute, Mount Sinai Hospital, Toronto; and* [4]*Heart and Stroke/Richard Lewar Centre of Excellence, University of Toronto, Toronto, Canada*

Submitted 23 August 2005; accepted in final form 28 October 2005

Nieman, Brian J., Ann M. Flenniken, S. Lee Adamson, R. Mark Henkelman, and John G. Sled. Anatomical phenotyping in the brain and skull of a mutant mouse by magnetic resonance imaging and computed tomography. *Physiol Genomics* 24: 154–162, 2006; doi:10.1152/physiolgenomics.00217.2005.—Since genetically modified mice have become more common in biomedical research as models of human disease, a need has also grown for efficient and quantitative methods to assess mouse phenotype. One powerful means of phenotyping is characterization of anatomy in mutant vs. normal populations. Anatomical phenotyping requires visualization of structures in situ, quantification of complex shape differences between mouse populations, and detection of subtle or diffuse abnormalities during high-throughput survey work. These aims can be achieved with imaging techniques adapted from clinical radiology, such as magnetic resonance imaging and computed tomography. These imaging technologies provide an excellent nondestructive method for visualization of anatomy in live individuals or specimens. The computer-based analysis of these images then allows thorough anatomical characterizations. We present an automated method for analyzing multiple-image data sets. This method uses image registration to identify corresponding anatomy between control and mutant groups. Within- and between-group shape differences are used to map regions of significantly differing anatomy. These regions are highlighted and represented quantitatively by displacements and volume changes. This methodology is demonstrated for a partially characterized mouse mutation generated by *N*-ethyl-*N*-nitrosourea mutagenesis that is a putative model of the human syndrome oculodentodigital dysplasia, caused by point mutations in the gene encoding connexin 43.

image processing; GJA1; connexin 43; oculodentodigital dysplasia.

GENETICALLY MODIFIED ANIMALS, especially mice, have become commonplace in biomedical research. Although the study of these animals opens new opportunities for understanding the biology of development and disease processes, it also introduces a need for efficient and reliable mouse characterization. Such characterization must be as objective and as extensive as possible, particularly since individual genetic mutations may produce unknown and unanticipated alterations in several developmental or physiological processes. A common phenotype symptomatic of such changes is abnormal anatomy or morphology since both developmental defects and functional deficiencies are commonly accompanied by anatomical changes. As a consequence, techniques for rapid anatomical characterization are highly beneficial to studies of mutant mice.

Medical imaging technologies are effective in depicting human anatomy and can likewise be used for anatomical phenotyping when adapted to the mouse scale (4, 14, 15, 27, 33, 36). These technologies have the advantage of being noninvasive and repeatable for longitudinal in vivo examinations. Furthermore, they provide superior three-dimensional and nondestructive visualization over large regions for fixed specimens compared with traditional sectioning. Imaging thus complements traditional pathology and histology, which offer higher resolution but are labor intensive and limited in anatomical coverage.

As with other phenotyping studies, thorough imaging studies require comparison of mouse populations, typically an anatomically normal control group and a mutant group. It is important that there be several mice in each group since anatomical differences should be assessed against inherent biological variability. Given that each individual three-dimensional image can be very large, comparison of an ensemble of images for subtle differences is not practical by traditional radiological observation. Furthermore, if more than one mutant, experimental condition, or time point is to be evaluated, then the task of systematic anatomical analysis can quickly become enormous. An automated protocol for the initial evaluation of mouse phenotypes would clearly be beneficial in identification of anatomical differences consistent over a mutant population.

To automate analysis of images, a means of computational image comparison is required. Image registration may be used in this capacity. The aim of registration is to find a corresponding anatomical location in a reference image for every location in the given image. When defined over the whole image, these correspondences completely capture the shape difference between two individuals. The displacement of a corresponding location between two images is represented by a vector, and the set of these vectors for a given image is a referred to as a deformation field. Deformation-based morphometry refers to the analysis of a group of deformation fields to identify significant anatomical changes between populations. Analyses of this kind have been applied in humans to establish, for example, anatomical differences dependent on gender and handedness (19), age (20), and schizophrenia (16).

In this paper, we implement deformation-based morphometry as a method of anatomical mouse phenotyping. The method greatly simplifies phenotyping analysis in two ways. First, average images are composed to represent each of the control and mutant mouse groups. This reduces the number of images that need to be examined. Second, significant anatomical changes are identified computationally as regions where intergroup deformations are large relative to the intragroup variations. These regions are subsequently highlighted as color

Article published online before print. See web site for date of publication (http://physiolgenomics.physiology.org).

Address for reprint requests and other correspondence: B. J. Nieman, Mouse Imaging Centre, Hospital for Sick Children, 555 Univ. Ave., Toronto, Ontario, Canada M5G 1X8 (e-mail: brian.nieman@sw.ca).

overlays on the average images. Thus group differences are summarized by two representative images with highlighted regions superimposed. The highlighted areas are not restricted to user-defined anatomical structures but instead represent a continuous voxel-by-voxel definition of change. This is advantageous because anatomical changes can be localized to substructures, and shape differences that affect multiple structures simultaneously can be properly visualized as a collective. The method is demonstrated in vivo with magnetic resonance (MR) imaging (MRI) and in situ after fixation with both MRI and micro-computed tomography (CT).

We applied this phenotyping method to a mouse with a mutation in the gap junction protein alpha 1 gene (*Gja1*), which encodes for connexin 43 (Cx43). Mutation of the *GJA1* gene in human patients is associated with an autosomal dominant condition called oculodentodigital dysplasia (37). It is characterized by abnormal development of the face, limbs, and dentition (6, 18, 21, 35, 39). Neurological symptoms have also been described, sometimes including paraparesis or quadriparesis, gait and bladder disturbances, and hyperreflexia (28). Several investigations of mice with modified *Gja1* expression have been reported, with a range of described phenotypes. In knockout animals, phenotypes include defects in the germ line and gonads (24) and cardiac malformation (38). Other reports include a mutation induced with *N*-ethyl-*N*-nitrosourea (ENU) that produces a severely truncated Cx43 and shows cardiac defects in homozygous mice similar to the knockout phenotype (45). Studies in heterozygous animals have also been described with mice showing increased susceptibility to lung cancer (1). Expression patterns also implicate a role for Cx43 in limb formation (31).

In this study, the mutant is referred to as the $Gja1^{Jrt}$ mouse. This mutant was generated by chemical mutagenesis with ENU (22, 32). Characterization of the $Gja1^{Jrt}$ mutant has revealed numerous abnormalities consistent with impaired gap-junction formation and oculodentodigital dysplasia. These include syndactyly, morphological and functional cardiac defects, reduced bone mineral density, and abnormal dentition (13). We examined this mouse model by both MRI and CT of the head and discovered anatomical phenotypes in the brain and skull.

MATERIALS AND METHODS

Animals. The $Gja1^{Jrt}$ mutant mouse (13) was generated by ENU mutagenesis at the Centre for Modeling Human Disease (Toronto, Ontario, Canada). Briefly, C57BL/6J male mice were treated with ENU and then bred with C3H/HeJ female mice. Offspring were screened for traits of interest (such as fused toes) and then bred to C3H/HeJ to test for heritability of this trait. Lines were maintained by breeding with C3H/HeJ females. Third-generation mice were used in these experiments, with unaffected littermates used as controls. Five mice were included in each of the control and mutant groups. In vivo images were performed at ~60 wk of age, and then animals were fixed for additional imaging. One in vivo image was judged to be of unsuitable quality for analysis, so only four control images were included in the in vivo data set. All animal protocols were approved by the Hospital for Sick Children Animal Care Committee.

Imaging protocols. All MRI was performed with multiple-mouse MRI (5). In this technique, several mice are imaged simultaneously in the same gradient set using multiple radiofrequency coils to increase image throughput. For in vivo brain images, mice were anesthetized with vaporized isoflurane (Baxter, Toronto, Canada) at 4% concentration during the induction phase and then at 0.8–1.0% concentration throughout the imaging session. Three-dimensional fast spin-echo images were acquired on a cartesian matrix with image parameters: 12 ms echo time, 900 ms repetition time, 36 ms effective echo time, eight echoes, two averages, 40 × 24 × 24 mm field-of-view and 384 × 208 × 208 matrix size for an imaging time of 2 h 45 min. The excitation tip angle was set to 40°. This improves signal efficiency and T_2-contrast by maintaining more magnetization longitudinally (34).

After acquisition of in vivo data, mice were fixed according to a protocol described previously (46). In this procedure, the mouse is anesthetized and an intravenous catheter (0.62-mm diameter) and needle are guided by high-frequency ultrasound (Vevo 660, Visual Sonics, Toronto, Canada) to puncture the left ventricle. Perfusion of saline and heparin is followed by 10% buffered formalin phosphate (Fisher Scientific, Nepean, Ontario, Canada). A contrast agent, gadopentetate dimeglumine (Magnevist, Berlex Canada, Quebec, Canada), was included in the perfusate solutions at 10 and 1 mM concentration in the heparin and formalin solutions, respectively; however, since the contrast agent does not cross the blood-brain barrier, it is not expected to significantly alter visualization of neuroanatomy. A simple multiple-mouse MRI three-dimensional spin-echo sequence was used to acquire head images of the fixed mice. Sequence parameters included 36 ms echo time, 550 ms repetition time, and 40 × 24 × 24 mm field-of-view and 512 × 300 × 300 matrix size for an imaging time of 13 h 45 min. In analogy to the partial excitation in the fast spin echo sequence, the excitation in the spin-echo sequence was set to maintain some magnetization longitudinally. However, the single 180°-refocusing pulse in the spin echo also serves as an inversion pulse. Because the magnetization must be returned to the positive longitudinal axis to be beneficial to signal efficiency and T_2-contrast, an overdriven excitation angle is selected. In these experiments, a flip angle of 140° was used.

All MRI data were acquired on a Varian INOVA console (Varian NMR Instruments, Palo Alto, CA) with a 7.0-T magnet (Magnex Scientific, Oxford, UK). The system is equipped with a 29-cm inner bore diameter gradient set (Tesla Engineering, Storrington, Sussex, UK) with 120-mT/m maximum amplitude and 870-μs rise time. The mouse-handling hardware to accommodate multiple lines of anesthesia, radio frequency coils, and monitoring equipment were described elsewhere (11). In vivo fast spin echo images were reconstructed using MATLAB software (MathWorks, Natick, MA) with echo amplitude corrections (7). All other reconstructions were performed on an SGI Onyx 3800 with 32 CPUs and 32 gigabytes of RAM (Silicon Graphics, Mountain View, CA). Images were resampled using tricubic interpolation to 100 and 80 μm isotropic voxels before analysis for the in vivo and fixed MR data sets, respectively.

After MR image acquisitions were complete, the fixed mice were decapitated for the purpose of skull structure visualization by micro-CT. Three-dimensional CT data sets were acquired using a MS-9 micro-CT scanner (GE Medical Systems, London, Ontario, Canada) (30) with the X-ray source at 80 kVp (mean energy of incident beam: 32 keV). Images were acquired in 2.5 h with 900 views and reconstructed on a 120-μm isotropic grid using the Feldkamp algorithm for cone-beam CT geometry (12). The computed images show calcified bone as highly intense regions against a relatively uniform dark background.

Image analysis. To visualize and compare data sets, average images were generated from each of the three imaging protocols for both control and mutant groups using the registration procedure described previously (25). In this method, an average image is composed from all members of the population. This average is formed through a series of registration steps. In the first step, the brains are normalized with respect to orientation, location, scale, and intensity. This removes image differences unrelated to biological variations such as translations and rotations and also provides estimates of global size differences. A common space is also defined to represent images in a spatially unbiased fashion (43, 44). A voxelwise average of the images in this orientation provides an initial average image estimate.

Subsequently, nonlinear registration of the individual images to the average provides a new set of images that allows creation of an improved average representation. This process is repeated iteratively at progressively finer resolutions until the final average is achieved, at which point correspondence is achieved by shifting individual image voxels. The resulting deformation field represents all such voxel displacements and encodes the shape differences between each image and the population average. The set of deformation fields from all images encodes the population variability. It is convenient to quantify this variability as an average over all voxels of the root mean square displacement (after subtraction of the mean group changes). This is calculated directly from the deformation fields and serves to assess the relative sensitivity of each image analysis.

The average control image for each imaging protocol was used as a reference for further analysis. Each image from the mutant population was registered to this reference using the same series of steps used to produce the control and mutant averages. Altogether, the complete set of deformation fields maps each image to its respective average as well as each mutant image to the control average. The various images and deformation fields for each protocol are represented schematically in Fig. 1, where lines between images represent the deformation fields. The deformation fields to the control average, labeled as $D_{C1–5}$ and $D_{M1–5}$ for the control and mutant data, respectively, are used for further analysis.

After generation of the average images and associated deformation fields, several differences between the mutant and control images were assessed. First of all, the size of the mutants was compared with the controls. This was accomplished by considering the overall scale factors determined in the initial linear registration steps. If the average mutant mouse is smaller or larger than the average control mouse, then significant deviations from unity will be apparent in the scale factors. The significance of scale differences was assessed by a Student's *t*-test of log-scale values. Second, anatomical phenotypes related to shape were recognized as mean displacements in the mutant deformation fields that are large compared with the displacements within each group. The regions of greatest interest can be visualized in this case by calculation of a Hotelling T^2 field (8, 40). This statistical map can be thought of as a mean squared displacement over variance quantity, so that large values of the Hotelling T^2 field indicate regions of significant change. Third and last in our assessment, local volume changes were estimated from the deformation fields by calculation of the determinant of the Jacobian matrix. Mean values in the mutant Jacobian maps that are outliers with respect to the inherent biological variability show relative size changes. The regions of greatest interest in this case are visualized using a Student's *t*-test of log-Jacobian values. Thus the problem of analyzing a many-image data set is reduced to considering only control and mutant average images with a Hotelling's T^2 field and log-Jacobian *t*-test field indicating the regions of most significant change.

Image processing was performed using in-house software. The packages AIR5.22 from the University of California, Los Angeles (43, 44), and ANIMAL from the Montreal Neurological Institute (10) were used for estimating linear and nonlinear deformations, respectively. Before analysis, all deformation fields were smoothed using a three-dimensional Gaussian kernel with full-width half-maximum equal to three image voxels (i.e., 0.3, 0.24, and 0.36 mm, respectively, for the in vivo MRI, fixed MRI and CT data sets). The analysis for each set of images required 10–15 h to run using ten 600-MHz processors on the SGI Onyx 3800. Note that a single high-end workstation with two processors operating at 2–3 GHz could also perform the analysis in roughly the same time frame.

RESULTS

The results of the imaging and average image generation are presented in Fig. 2 for each of the different modalities. A complete sample of image data from an individual mouse is shown in the first row for all three image protocols. The next two rows show the control and mutant average images. Note that the average generation and analysis were limited to the brain volume in the MR data and excluded surrounding muscle, eyes, and other tissue. Similarly, the CT analysis was restricted to craniofacial regions and did not include the mandible, teeth, or spine. The average images show an apparent improvement in image quality compared with the individual image. We have found this to be typical of averages generated for inbred mouse strains, where the population is genetically homogeneous (9, 25).

The first step in our analysis was to consider the relative size of mutants and controls. Overall, mutant mice were observed to be smaller than their control counterparts. Before in vivo imaging, control mice weighed 31 $\pm$ 4 g, whereas mutant mice weighed only 20 $\pm$ 2 g. Thus it was expected that some scale differences would be evident in the registration analysis. The average scale factors generated by the linear registration algorithm are given in Table 1. By definition, the control scale factors average to unity. The most obvious scale changes appear in the mutant skull data, particularly in the anterior-posterior direction. Manual measurements confirmed the trends indicated in Table 1 and provide a quantitative measure of image geometry. Skull dimensions in the average control image were measured to be 10.9 mm (across the squamosal bones), 23.9 mm (from the posterior of the occipital bone to the anterior of the nasal bones), and 7.5 mm (from the inferior face of the basiocciptal bone to the superior face of the parietal bones). Equivalent average mutant skull dimensions were measured to be 10.2, 20.6, and 7.5 mm, respectively. This is equivalent to scale factors of 0.94, 0.86, and 1.0; note that an exact correspondence between these scales and those in Table

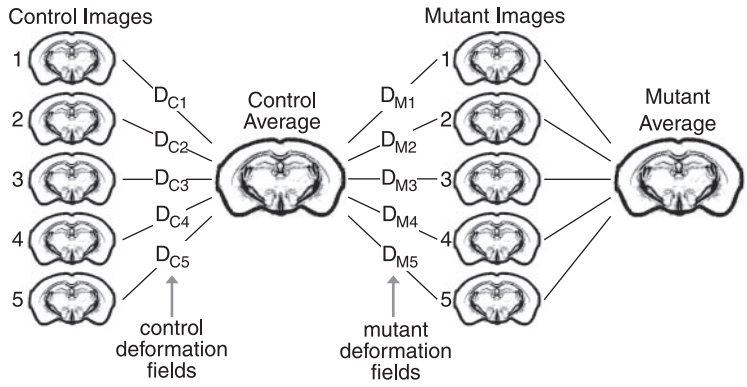

Fig. 1. Schematic diagram indicating the control images, mutant images, control average image, and mutant average image. Lines between each of the images represent deformation fields determined by nonlinear registration. The deformation fields to the control average (labeled $D_{C1–5}$ and $D_{M1–5}$ for the control and mutant groups, respectively) were used for image analysis and generation of statistical maps.

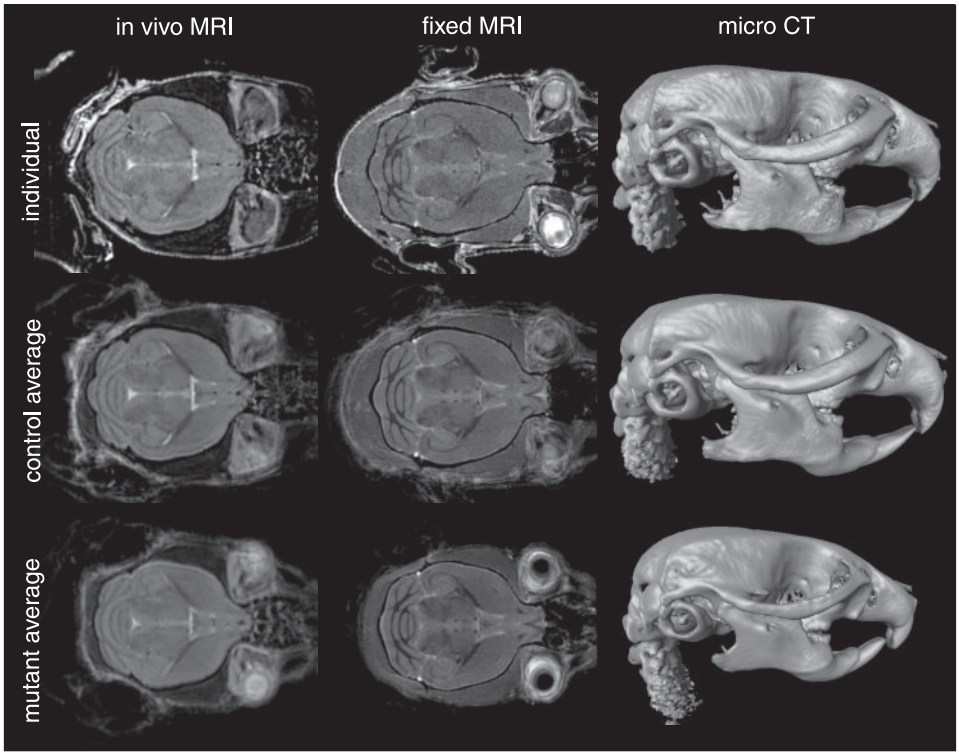

Fig. 2. Image acquisition and average image generation results. *Top*: images from a single individual for each of the three imaging protocols. *Middle* and *bottom*: control (*middle*) and mutant (*bottom*) average images as generated by the protocol given by Kovacevic et al. (25). MRI, magnetic resonance imaging; CT, computed tomography.

1 is not expected since these are by nature single-point measurements, whereas the registration-derived scales account for the entire skull volume. The MRI data also indicated changes in the size of control and mutant brains, particularly in the fixed mouse data. Manual volume measurements of the brain confirm the size change. The average control brains were calculated to have volumes of 490 and 500 mm^3 for the in vivo and fixed MR brains, respectively. Mutant mice were found to have smaller brains, measuring 450 and 440 mm^3.

Results of the deformation field analysis for the MR data are shown in Fig. 3. The left column shows the in vivo results and the right column shows the fixed results. From *top* to *bottom*, Fig. 3 displays the control average images, the mutant average images after 12-parameter linear registration, the control average images with an overlay of vectors at ×2 scale showing the mean deformation field to the mutant images, the Hotelling T^2 statistical field calculated from the deformation fields, the magnitude of mean mutant deformations masked by setting a threshold on the Hotelling T^2 field, and finally the determinants of the Jacobian matrices as masked by the Student's *t*-test of log-Jacobian values. The thresholds for the regions of interest in Fig. 3, *I–L*, were determined according to the false discovery rate (FDR) (2, 3, 17). The permitted FDR was adjusted in each case until the most prominent features of the statistical map, either the Hotelling's T^2 or the *t*-test field, were above threshold. For the MRI data, relatively high FDR values were necessary (20, 15, 35, and 25% for Fig. 3, *I–L*, respectively). This indicates that the changes are relatively subtle with respect to biological variability and image resolution. The deformation field variability was characterized by calculation of the average root mean square displacement, determined to be 160 and 140 μm for the in vivo and fixed data, respectively. Calculated values within each of the mutant and control groups were identical.

From the vector fields in Fig. 3, *E* and *F*, the regions with the largest displacements appear to be within the cerebellum and the forebrain, just posterior to and including the olfactory bulb. The magnitude displacement overlays provided in Fig. 3, *G* and *H*, confirm this impression, indicating that the most significant and largest continuous region of shape change is in the posterior and superior portion of the cerebellum. Displacements of ~400 μm are evident in this region. The cerebellum

Table 1. *Relative sizes in the mutant and control for three imaging protocols*

Imaging Protocol	Mouse Group	Left-Right Scale	Anterior-Posterior Scale	Inferior-Superior Scale	Scale Product
In vivo MRI	Mutant	0.97±0.01	0.95±0.04	1.03±0.02	0.95±0.04
	Control	1.00±0.04	1.00±0.06	1.00±0.07	1.00±0.09
Fixed MRI	Mutant	0.94±0.03*	0.92±0.05*	1.01±0.02	0.88±0.02*
	Control	1.00±0.03	1.00±0.05	1.00±0.03	1.00±0.03
Micro-CT	Mutant	0.91±0.01*	0.88±0.02*	0.96±0.01*	0.76±0.03*
	Control	1.00±0.01	1.00±0.02	1.00±0.03	1.00±0.02

Scale values are means ± SD for each mouse and were generated by linear registration to the control average image. The product of the three scale factors were multiplied together and then averaged to yield a scale product representative of volume changes. MRI, magnetic resonance imaging; CT, computed tomography. *$P < 0.05$ using a Student's *t*-test of log-scale values.

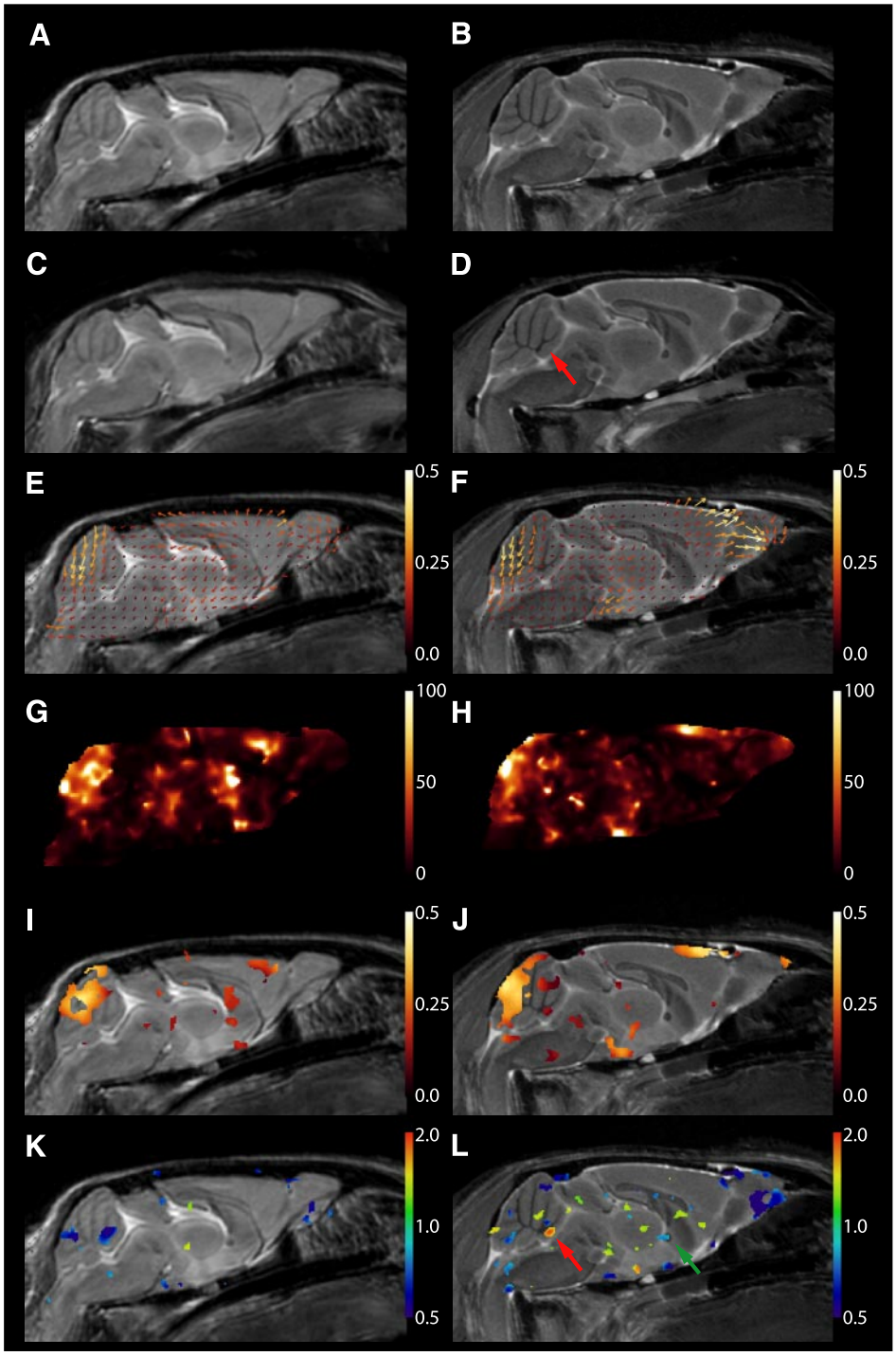

Fig. 3. Highlighted analysis results from the in vivo and fixed MRI data sets. In vivo results are shown on *left* (*A*, *C*, *E*, *G*, *I*, and *K*) and fixed results are shown on *right* (*B*, *D*, *F*, *H*, *J*, and *L*). *A* and *B*: control average images. *C* and *D*: mutant average images following 12-parameter linear registration to the respective control averages. The mean vector deformations from the control averages to the mutant averages are shown at ×2 scale projected onto the sagittal slice of the control averages in *E* and *F*. Most of the deformations were found to be in the sagittal plane, so the vectors shown provide a faithful representation of the shape changes. Vectors are color coded by their magnitude (in mm). Using the deformations, a Hotelling T^2 statistical map was generated as shown in *G* and *H*. The regions of most significant change were identified by thresholding this map at a value corresponding to false discovery rates of 20 and 15% for *I* and *J*, respectively. The magnitude of the mean mutant deformation field (in mm) is shown in these regions as a color overlay. At *bottom*, the deformation fields were used to calculate Jacobian values, which are displayed as a color overlay. Region selection was established using a Student's *t*-test of log-Jacobian values and false discovery rates of 35 and 25%. The red arrow in *D* and *L* indicate an apparent change in the branching of the cerebellar folia. The green arrow highlights volume change at the anterior commissure.

displacements appear to occur for the most part without producing volume changes, as evidenced by Fig. 3, *I* and *J*. The most obvious region of volume change is actually in the olfactory bulb (from the fixed mouse data in Fig. 3*L*). This can be observed by comparison of Fig. 3, *B* and *D*. A similar trend can be seen in the in vivo data in Fig. 3, *A* and *C*, but does not reach significance in the in vivo Jacobian calculation. Of additional interest in the fixed data is the anterior region of the cerebellar folia. A change in the position of folia branching appears to occur with neighboring size adjustments evident in the Jacobian data (Fig. 3, *D* and *L*, red arrows). This feature was inspected individually in all of the fixed mouse images and found to be consistently present in all the mutant images but absent in all the control images. Additionally, the anterior commissure is highlighted in the fixed mouse data, showing a size decrease (Fig. 3*L*, green arrow). This feature is much more obvious in a horizontal slice as shown in Fig. 4. The Jacobian values show a consistent decrease all along the horseshoe path of the anterior commissure (Fig. 4*C*). Manual measurements in the control average image and mutant average image (after

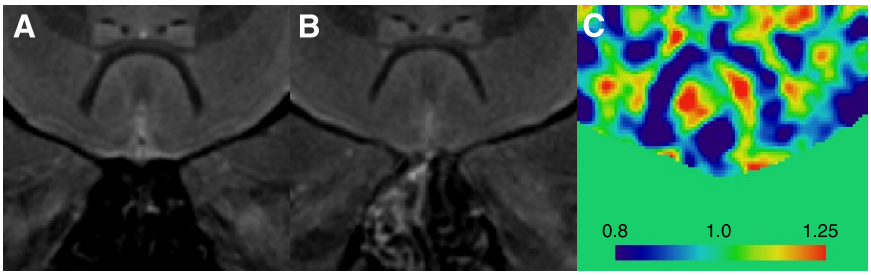

Fig. 4. Horizontal view of the anterior commissure in the fixed mouse data set. *A* and *B*: anterior commissure in the average control image and average mutant image (*A* and *B*, respectively). *C*: calculated Jacobian values are shown. A distinct decrease in size is seen along the path of the anterior commissure.

12-parameter registration) indicate an overall decrease in anterior commissure width from ~320 to 240 μm. Although this change is considered to be at the limit of detection, being only one image voxel, the Jacobian data appears consistent with this measurement. Overall, the highlighted features in the MR data were sufficiently reliable that images could be identified as either control or mutant based on individual features.

Figure 5 shows the results of the deformation field analysis for the CT data. This data showed both more sizeable and more significant mutant differences. In this case, surface renderings of the three-dimensional average images are shown in all panels except for the sagittal cut in Fig. 5*C*. Similar to the MR data, Fig. 4 shows the control average, the mutant average following 12-parameter linear registration, the control average in the sagittal plane with a projection of the mean mutant deformation vectors at ×1 scale, the Hotelling T^2 statistical field calculated from the deformation fields, the magnitude of deformations as masked by the Hotelling T^2 field, and also the determinant of the Jacobian matrix as masked by the Student's *t*-test of log-Jacobian values. In the case of the CT data, much smaller FDR threshold values were used, 1% and 5% for Fig. 5, *E* and *F*, respectively. This indicates a high level of significance and suggests both prominent and consistent anatomical changes. Background variability was characterized by an average root mean square displacement of 220 μm and was identical within the control and mutant groups.

Deformations as large as 1 mm are observed, particularly in the facial region along the zygomatic arch where both a thinning and an inward displacement occur as well as across the nasal bones where a distinct depression is evident. Additional smaller outward displacements are also indicated on the frontal and occipital bones. The Jacobian data show that there are accompanying volume changes with these displacements (Fig. 5*F*). This is most obvious in the anterior portion of the zygomatic arch and along the suture between the parietal and interoccipital bones. The latter can also be appreciated from the MRI data (i.e., Fig. 3, *A–D*). In fact, the changes in the skull shape were found to be consistent with those of the brain, with significant deformations in regions near the olfactory bulb, forebrain, and cerebellum. However, as described, the CT data further revealed large regions of facial deformation.

DISCUSSION

We note that the *Gja1*^{Jrt} phenotypes discussed in this paper were highlighted in a simple and automated fashion. Large three-dimensional data sets were simplified to small regions-of-interest with further quantification provided in these areas. A large number of images were combined into a compact and manageable representation. In this manner, the analysis "handwork" was restricted to verification and description of the identified phenotypes. This makes anatomical phenotyping a much simpler process, as demonstrated here in the *Gja1*^{Jrt} mutant. This type of method is expected to improve the efficiency of data analysis in mouse phenotyping studies and will render such studies more interpretable.

Overall, the phenotyping method was successful for all three of the different imaging protocols presented in this paper, namely in vivo MRI, fixed MRI, and micro-CT. However, the resolution and accuracy of phenotyping results did vary from one protocol to another. Clearly, the number, type, and quality of images in the data set influence the outcome of any phenotyping experiment. The analysis method described here necessitates a minimum of eight mouse images; the Hotelling T^2 calculation requires six degrees of freedom to estimate a covariance matrix plus an additional degree of freedom for each the control and mutant averages. However, the addition of more images will always render a study more powerful, enabling more subtle phenotypes, if present, to be unambiguously detected. Careful selection of the number of mice to include in a study will thus require consideration of the desired scale of phenotype resolution compared with the level of biological variability and image resolution. For exploratory investigations, 10–12 mice are reasonable in our experience. Improved phenotype detection can also be achieved by the choice of an appropriate imaging modality. For instance, in the present study, the CT data demonstrated a much more pronounced differences than the MR data despite the larger background variability in the CT data; the improved detection by CT is due to the large craniofacial defects in the *Gja1*^{Jrt} mutant compared with relatively subtle soft tissue deformations. The detection capability of an imaging modality is a strong function of the particular phenotype of interest. Of course, without a priori knowledge of the mouse phenotype, selection of an optimal imaging modality may not be possible. Beyond the biological variation, detection is inherently limited by image quality. Image resolution, contrast-to-noise ratio, and artifact levels are all important factors. For instance, the in vivo data was both less significant and less informative than the fixed MR results. This was in part due to the reduced number of control mice (four instead of five) but also a function of the lower resolution and increased artifact level inherent to in vivo data.

In fact, the improved detection apparent in the fixed MR images makes this an attractive protocol for phenotyping. However, it is important to note that the fixed images came at the cost of imaging sessions that were five times longer and would clearly be inappropriate for any form of longitudinal study. Thus, for future studies, the nature of the mouse mutation and the desired resolution of anatomical information will guide the design of an imaging protocol. If fixed mice are acceptable, then the improved image quality increases the

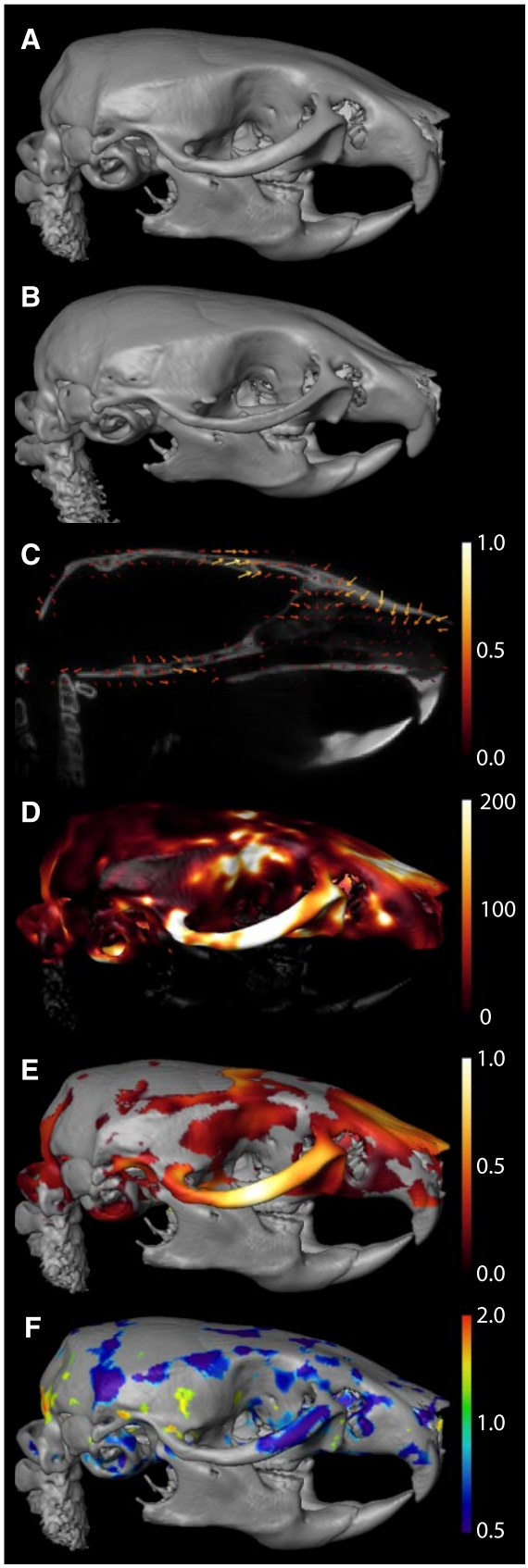

likelihood of detecting anatomical phenotypes. The close correspondence of volume measurements between the in vivo and in situ fixed MR data (within 3% in this study) suggests that this increased phenotyping capability does not necessarily compromise quantitation. In this sense, in situ fixation is far more desirable than traditional methods of ex vivo fixation, in which tissue shrinkage or deformation can significantly alter results (29). Conversely, ongoing improvements in imaging protocols continue to increase the resolution and reduce the artifact level of in vivo scans. For instance, high-resolution cine MR images of the beating heart can be acquired (41, 42). These advances allow the methodology presented here to detect more subtle phenotypes with live image data and to expand to other parts of the body otherwise obscured by physiological motion.

Other factors may also affect the performance of this phenotyping method. For instance, nonlinear registration inherently assumes that there is corresponding anatomy in both the control and mutant groups. Phenotypes where large structures are introduced or removed would thus be likely to produce unreliable results. This represents a possible limitation of the algorithm. However, we note that such phenotypes are more likely to be obvious on radiological observation. Consequently, the phenotyping procedure as presented here still provides an important simplification by reducing the number of images to be examined. Mutations that produce subtle changes in three-dimensional shape or size are the ones less easily identified by manual observation. The analysis presented here is intended to more effectively identify the latter phenotypes.

This study demonstrates that the quantification of anatomical phenotypes enables a precise description of mutant abnormalities. However, characterization of the phenotype does not reveal the associated mechanisms of malformation. The abnormalities observed by imaging in the brain and skull of the *Gja1*^{Jrt} mouse raise an interesting question about interactions during brain and skull development. Further investigation would be required to understand the dominant factors that determine the size and shape of the head. In the case of the *Gja1* gene, supplemental information is already available. Previous reports of knockout mice lacking Cx43 indicate that it plays an important role in osteoblast function and proper ossification (26). Furthermore, the migration of cells from the neural crest, which contributes to the growth of the cranial vault, is modified in a Cx43 dose-dependent fashion (23). This suggests that impaired Cx43 function leads to the improper formation of the skeletal elements in the head as observed here by micro-CT. The MR data also indicates changes in the overall brain shape that are consistent and possibly secondary

Fig. 5. Highlighted analysis results from the CT data set. *A*: control average image. *B*: mutant average image after 12-parameter linear registration to the control average image. *C*: mean vector deformations from the control average to the mutant images shown at ×1 scale. They are projected onto the sagittal plane of the control average image and color coded according to their magnitude (in mm). Vector deformations were mostly restricted to the sagittal plane in this slice. The regions of most significant deformation were determined by calculation of a Hotelling T^2 field (shown in *D*) and then thresholding at a value corresponding to a 1% false discovery rate. *E*: magnitude of the mean mutant deformation field (in mm) is shown in the regions of significance as a color overlay. *F*: Jacobian values calculated from the deformation fields are shown by a color overlay. Region selection was established based on a Student's *t*-test of log-Jacobian values and a 5% false discovery rate.

to the bone abnormalities. Additionally, however, local unrelated neuroanatomical changes are present. Thus, although it seems that the skull development is certainly affected, whether brain abnormalities also contribute to the changes in head shape is not clear.

In conclusion, in this paper, we have presented a technique for detection and analysis of anatomical phenotypes in the mouse using three-dimensional image data. This technique greatly reduces the complications of analyzing multiple specimen anatomical data by representing populations with an average image and highlighting regions where significant changes have occurred. The method has been implemented successfully with in vivo MRI, in situ MRI, and micro-CT for the comparison of mutant and normal mouse anatomy in the head. This technique uncovered important structural changes in the skull and brain of the *Gja1*^{Jrt} mutant mouse and is expected to be appropriate for any biological study in which anatomy is used to identify differences between control and experimental groups.

ACKNOWLEDGMENTS

The authors gratefully acknowledge Victoria Bonn and Lisa Yu for technical assistance as well as the Centre for Modeling Human Disease for making the *Gja1*^{Jrt} mouse available for study.

GRANTS

Funding was provided by the Canada Foundation for Innovation/Ontario Innovation Trust, Ontario Research and Development Challenge Fund, and the National Institutes of Health. Brian Nieman is recipient of a Canada Graduate Scholarship. Mark Henkelman is recipient of a Canada Research Chair in Imaging.

REFERENCES

1. **Avanzo JL, Mesnil M, Hernandez-Blazquez FJ, Mackowiak II, Mori CMC, da Silva TC, Oloris SCS, Garate AP, Massironi SMG, Yamasaki H, and Dagli MLZ.** Increased susceptibility to urethane-induced lung tumors in mice with decreased expression of connexin43. *Carcinogenesis* 25: 1973–1982, 2004.
2. **Benjamini Y and Hochberg Y.** Controlling the false discovery rate—a practical and powerful approach to multiple testing. *J Roy Stat Soc B Met* 57: 289–300, 1995.
3. **Benjamini Y and Yekutieli D.** The control of the false discovery rate in multiple testing under dependency. *Annu Stat* 29: 1165–1188, 2001.
4. **Bentley MD, Ortiz MC, Ritman EL, and Romero JC.** The use of microcomputed tomography to study microvasculature in small rodents. *Am J Physiol Regul Integr Comp Physiol* 282: R1267–R1279, 2002.
5. **Bock NA, Konyer NB, and Henkelman RM.** Multiple-mouse MRI. *Magn Reson Med* 49: 158–167, 2003.
6. **Brueton LA, Huson SM, Farren B, and Winter RM.** Oculodentodigital dysplasia and type-III syndactyly—separate genetic entities or disease spectrum. *J Med Genet* 27: 169–175, 1990.
7. **Busse RF, Riederer SJ, Fletcher JG, Bharucha AE, and Brandt KR.** Interactive fast spin-echo imaging. *Magn Reson Med* 44: 339–348, 2000.
8. **Cao J and Worsley KJ.** The detection of local shape changes via the geometry of Hotelling's T-2 fields. *Ann Stat* 27: 925–942, 1999.
9. **Chen XJ, Kovacevic N, Lobaugh NJ, Sled JG, Henkelman RM, and Henderson JE.** Neuroanatomical differences between mouse strains as shown by high-resolution 3D MRI. *Neuroimage*. In press.
10. **Collins DL, Evans AC.** Animal: validation and applications of nonlinear registration-based segmentation. *Intern J Pattern Recognit Artif Intell* 11: 1271–1294, 1997.
11. **Dazai J, Bock NA, Nieman BJ, Davidson LM, Henkelman RM, and Chen XJ.** Multiple mouse biological loading and monitoring system for MRI. *Magn Reson Med* 52: 709–715, 2004.
12. **Feldkamp LA, Davis LC, and Kress JW.** Practical cone-beam algorithm. *J Opt Soc Am A Opt Image Sci Vis* 1: 612–619, 1984.
13. **Flenniken AM, Osborne LR, Anderson N, Ciliberti N, Fleming C, Gittens JEI, Gong XQ, Kelsey LB, Lounsbury C, Moreno L, Nieman BJ, Peterson K, Qu D, Roscoe W, Shao Q, Tong D, Veitch GIL, Voronina I, Vukobradovic I, Wood GA, Zhu Y, Zirngibl RA, Aubin JE, Bai D, Bruneau BG, Grynpas M, Henderson JE, Henkelman RM, McKerlie C, Sled JG, Stanford WL, Laird DW, Kidder GM, Adamson SL, and Rossant J.** A *Gja1* missense mutation in a mouse model of oculodentodigital dysplasia (ODDD). *Development* 132: 4375–4386, 2005.
14. **Foster FS, Pavlin CJ, Harasiewicz KA, Christopher DA, and Turnbull DH.** Advances in ultrasound biomicroscopy. *Ultrasound Med Biol* 26: 1–27, 2000.
15. **Fowler JS, Volkow ND, Wang GJ, Ding YS, and Dewey SL.** PET and drug research and development. *J Nucl Med* 40: 1154–1163, 1999.
16. **Gaser C, Volz HP, Kiebel S, Riehemann S, and Sauer H.** Detecting structural changes in whole brain based on nonlinear deformations—application to schizophrenia research. *Neuroimage* 10: 107–113, 1999.
17. **Genovese CR, Lazar NA, and Nichols T.** Thresholding of statistical maps in functional neuroimaging using the false discovery rate. *Neuroimage* 15: 870–878, 2002.
18. **Gillespie FD.** Hereditary syndrome—dysplasia oculodentodigitalis. *Arch Ophthalmol* 71: 187–192, 1964.
19. **Good CD, Johnsrude I, Ashburner J, Henson RN, Friston KJ, and Frackowiak RS.** Cerebral asymmetry and the effects of sex and handedness on brain structure: a voxel-based morphometric analysis of 465 normal adult human brains. *Neuroimage* 14: 685–700, 2001.
20. **Good CD, Johnsrude IS, Ashburner J, Henson RN, Friston KJ, and Frackowiak RS.** A voxel-based morphometric study of ageing in 465 normal adult human brains. *Neuroimage* 14: 21–36, 2001.
21. **Gorlin RJ, Meskin LH, and St Geme JW.** Oculodentodigital dysplasia. *J Pediatr* 63: 69–75, 1963.
22. **Hrabe de Angelis MH, Flaswinkel H, Fuchs H, Rathkolb B, Soewarto D, Marschall S, Heffner S, Pargent W, Wuensch K, Jung M, Reis A, Richter T, Alessandrini F, Jakob T, Fuchs E, Kolb H, Kremmer E, Schaeble K, Rollinski B, Roscher A, Peters C, Meitinger T, Strom T, Steckler T, Holsboer F, Klopstock T, Gekeler F, Schindewolf C, Jung T, Avraham K, Behrendt H, Ring J, Zimmer A, Schughart K, Pfeffer K, Wolf E, and Balling R.** Genome-wide, large-scale production of mutant mice by ENU mutagenesis. *Nat Genet* 25: 444–447, 2000.
23. **Huang GY, Cooper ES, Waldo K, Kirby ML, Gilula NB, and Lo CW.** Gap junction-mediated cell-cell communication modulates mouse neural crest migration. *J Cell Biol* 143: 1725–1734, 1998.
24. **Juneja SC, Barr KJ, Enders GC, and Kidder GM.** Defects in the germ line and gonads of mice lacking connexin43. *Biol Reprod* 60: 1263–1270, 1999.
25. **Kovacevic N, Henderson JT, Chan E, Lifshitz N, Bishop J, Evans AC, Henkelman RM, and Chen XJ.** A three-dimensional MRI atlas of the mouse brain with estimates of the average and variability. *Cereb Cortex* 15: 639–645, 2005.
26. **Lecanda F, Warlow PM, Sheikh S, Furlan F, Steinberg TH, and Civitelli R.** Connexin43 deficiency causes delayed ossification, craniofacial abnormalities, and osteoblast dysfunction. *J Cell Biol* 151: 931–944, 2000.
27. **Lecomte R, Cadorette J, Richard P, Rodrigue S, and Rouleau D.** Design and engineering aspects of a high-resolution positron tomograph for small animal imaging. *IEEE Trans Nucl Sci* 41: 1446–1452, 1994.
28. **Loddenkemper T, Grote K, Evers S, Oelerich M, and Stogbauer F.** Neurological manifestations of the oculodentodigital dysplasia syndrome. *J Neurol* 249: 584–595, 2002.
29. **Ma Y, Hof PR, Grant SC, Blackband SJ, Bennett R, Slatest L, McGuigan MD, and Benveniste H.** A three-dimensional digital atlas database of the adult C57BL/6J mouse brain by magnetic resonance microscopy. *Neuroscience* 135: 1203–1215, 2005.
30. **Marxen M, Thornton MM, Chiarot CB, Klement G, Koprivnikar J, Sled JG, and Henkelman RM.** MicroCT scanner performance and considerations for vascular specimen imaging. *Med Phys* 31: 305–313, 2004.
31. **Meyer RA, Cohen MF, Recalde S, Zakany J, Bell SM, Scott WJ Jr, and Lo CW.** Developmental regulation and asymmetric expression of the gene encoding Cx43 gap junctions in the mouse limb bud. *Dev Genet* 21: 290–300, 1997.
32. **Nadeau JH, Balling R, Barsh G, Beier D, Brown SD, Bucan M, Camper S, Carlson G, Copeland N, Eppig J, Fletcher C, Frankel WN, Ganten D, Goldowitz D, Goodnow C, Guenet JL, Hicks G, Hrabe de AM, Jackson I, Jacob HJ, Jenkins N, Johnson D, Justice M, Kay S, Kingsley D, Lehrach H, Magnuson T, Meisler M, Poustka A, Rinchik EM, Rossant J, Russell LB, Schimenti J, Shiroishi T, Skarnes WC, Soriano P, Stanford W, Takahashi JS, Wurst W, and Zimmer A.**

Sequence interpretation. Functional annotation of mouse genome sequences. *Science* 291: 1251–1255, 2001.
33. **Nieman BJ, Bock NA, Bishop J, Chen XJ, Sled JG, Rossant J, and Henkelman RM.** Magnetic resonance imaging for detection and analysis of mouse phenotypes. *NMR Biomed* 18: 447–468, 2005.
34. **Nieman BJ, Bock NA, Bishop J, Sled JG, Chen XJ, and Henkelman RM.** Fast spin-echo for multiple mouse MR phenotyping. *Magn Reson Med* 54: 532–537, 2005.
35. **Patton MA and Laurence KM.** 3 new cases of oculodentodigital (ODD) syndrome: development of the facial phenotype. *J Med Genet* 22: 386–389, 1985.
36. **Paulus MJ, Gleason SS, Easterly ME, and Foltz CJ.** A review of high-resolution X-ray computed tomography and other imaging modalities for small animal research. *Lab Anim* 30: 36–45, 2001.
37. **Paznekas WA, Boyadjiev SA, Shapiro RE, Daniels O, Wollnik B, Keegan CE, Innis JW, Dinulos MB, Christian C, Hannibal MC, and Jabs EW.** Connexin 43 (GJA1) mutations cause the pleiotropic phenotype of oculodentodigital dysplasia. *Am J Hum Genet* 72: 408–418, 2003.
38. **Reaume AG, De Sousa PA, Kulkarni S, Langille BL, Zhu D, Davies TC, Juneja SC, Kidder GM, and Rossant J.** Cardiac malformation in neonatal mice lacking connexin43. *Science* 267: 1831–1834, 1995.
39. **Schuller MG, Barnett ML, Strassburger K, Friedman DL, and Sonnenberg EM.** Oculodentodigital dysplasia. *Oral Surg Oral Med Oral Pathol Oral Radiol Endod* 61: 418–421, 1986.
40. **Thompson PM, MacDonald D, Mega MS, Holmes CJ, Evans AC, and Toga AW.** Detection and mapping of abnormal brain structure with a probabilistic atlas of cortical surfaces. *J Comput Assist Tomogr* 21: 567–581, 1997.
41. **Wiesmann F, Ruff J, Hiller KH, Rommel E, Haase A, and Neubauer S.** Developmental changes of cardiac function and mass assessed with MRI in neonatal, juvenile, and adult mice. *Am J Physiol Heart Circ Physiol* 278: H652–H657, 2000.
42. **Wiesmann F, Szimtenings M, Frydrychowicz A, Illinger R, Hunecke A, Rommel E, Neubauer S, and Haase A.** High-resolution MRI with cardiac and respiratory gating allows for accurate in vivo atherosclerotic plaque visualization in the murine aortic arch. *Magn Reson Med* 50: 69–74, 2003.
43. **Woods RP, Grafton ST, Holmes CJ, Cherry SR, and Mazziotta JC.** Automated image registration: I. General methods and intrasubject, intramodality validation. *J Comput Assist Tomogr* 22: 139–152, 1998.
44. **Woods RP, Grafton ST, Watson JD, Sicotte NL, and Mazziotta JC.** Automated image registration: II. Intersubject validation of linear and nonlinear models. *J Comput Assist Tomogr* 22: 153–165, 1998.
45. **Yu Q, Shen Y, Chatterjee B, Siegfried BH, Leatherbury L, Rosenthal J, Lucas JF, Wessels A, Spurney CF, Wu YJ, Kirby ML, Svenson K, and Lo CW.** ENU induced mutations causing congenital cardiovascular anomalies. *Development* 131: 6211–6223, 2004.
46. **Zhou YQ, Davidson L, Henkelman RM, Nieman BJ, Foster FS, Yu LX, and Chen XJ.** Ultrasound-guided left-ventricular catheterization: a novel method of whole mouse perfusion for microimaging. *Lab Invest* 84: 385–389, 2004.